

New numerical methods for the computation of the self-force around Black Holes

Master Thesis



Author:

Pol Pastells i Vilà

Director:

Dr. Carlos F. Sopuerta (ICE, CSIC and IEEC)

Master's Degree in Modeling for Science and Engineering

Bellaterra, June 2021

Abstract

The self-force problem arises in the description of the motion of particles under the action of physical fields. It has to do with the singularities that emerge when we estimate the action of the field created by a particle on its own motion. In this work we present a new method for the computation of the self-force acting on a particle moving under the influence of a scalar field in the spacetime geometry of a non-rotating (Schwarzschild) Black Hole.

Acknowledgments

I would like to thank Dr. Carlos Sopena for his guidance and patience during the last months, as well as my friends and family for their continuous support.

Contents

1	Introduction	4
2	EMRIs driven by a Scalar Self-Force	7
3	The Particle-without-Particle Formulation	10
4	PwP in the Frequency Domain	12
4.1	Grid Structure for the Numerical Computations	14
4.2	Hyperboloidal Compactification in Schwarzschild Spacetime	16
4.3	Method of Extended Homogeneous Solutions	19
4.4	Numerical implementation	22
5	Code implementation	25
5.1	Code structure	25
5.2	Python	27
5.3	Julia	27
5.4	ODE example	28
6	Results	29
7	Conclusions	30
A	Spherical Harmonics	32
B	Geodesic Particle motion	32
C	Hyperboloidal Compactification Expressions	34
	References	35

List of Figures

1	GW sources in the frequency range of LISA, compared with its sensitivity for a 3-arm configuration (<i>credit [7]</i>).	5
2	Schematic representation of the PwP formulation. The field equations with singular source terms become homogeneous equations at each side of the particle worldline, together with a set of jump conditions to communicate their solutions.	10
3	Schematic representation of the structure of the domains used in the frequency-domain solution of the scalar field equations.	16
4	Penrose-Carter diagram of the hyperboloidal compactification.	17
5	Schematic structure of the software project. Each node represents a different file, with the objects ending in brackets being functions, while the arrows show the dependencies of each file. Note that we do not show the utils file, used in both “Self-force” and “class_SF_Physics”.	26
6	Homogeneous solution $\hat{R}_{\ell mn}^{\pm}$ (real part) examples, with $\ell, m, n =$ (a) 0,0,3 at the HD, (b) 0,0,0 at the ID, note the exponential growth; (c) 2,2,16 at the HD, (d) 2,2,2 at the ID.	29
7	Convergence of the first ℓm -modes.	30

1 Introduction

Gravitational waves (GWs) are a natural phenomenon, predicted by Einstein’s General Relativity (GR) in 1916, and first observed experimentally in 2015 [1]. Einstein’s field equations describe the nonlinear relation and dynamics of matter and energy with the spacetime geometry. Time changing distributions of energy and momentum generate spacetime curvature ripples, GWs, that propagate across the Universe at the speed of light. They interact weakly with matter, unlike electromagnetic waves, carrying information across the Universe with barely any distortion, making them interesting as a new source for observational astrophysics and cosmology. Although the detectable events that generate GWs emit massive amounts of energy, they are usually many light-years away from us, requiring incredibly precise technology for their detection.

Ever since the groundbreaking discoveries of GWs by the LIGO-Virgo Collaboration [1, 2], GW astronomy has become a fast-growing field. Direct observation of binary Black Holes (BH), BH–Neutron Star (NS) and NS–NS mergers have led to profound advances in the understanding of the gravitational two-body problem. Nevertheless, ground-based detectors are not expected to be sensible to low-frequency GWs (below 1 Hertz). At lower frequencies, surface seismic waves [3] and stochastic gravity-gradient noise [4] become important. The first can be avoided by building underground detectors, like KAGRA [5] or the Einstein telescope [6], and some methods may even be able to compensate for the second, but ultimately space-based detectors must be used to surpass this barrier. The future LISA mission [7] will be an all-sky observatory, with sensitivity in a band from 10^{-4} Hz to 1 Hz. These low-frequency waves will allow for the detection of systems of BHs with masses ranging from a few M_{\odot} to $10^8 M_{\odot}$ (see Fig. 1).

Extreme-Mass-Ratio Inspirals (EMRIs) [8–10] are expected to be one of the main sources of GWs for the LISA observatory. EMRIs are binary systems, in which a stellar compact object (SCO) spirals into a (super) Massive BH (MBH). MBHs have masses of the order $M_{\bullet} \sim 10^{5-7} M_{\odot}$, while the typical mass for a SCO is $m_{*} \sim 1 - 50 M_{\odot}$. Therefore, EMRIs have a mass ratio $M_{\bullet}/m_{*} \sim 10^{3-7}$. In the regime where the dynamics is driven by GW emission, the SCO inspirals into the MBH, sweeping through the LISA frequency band and mapping the MBH spacetime onto the structure of the GWs in great detail. Orbiting for years before merging,

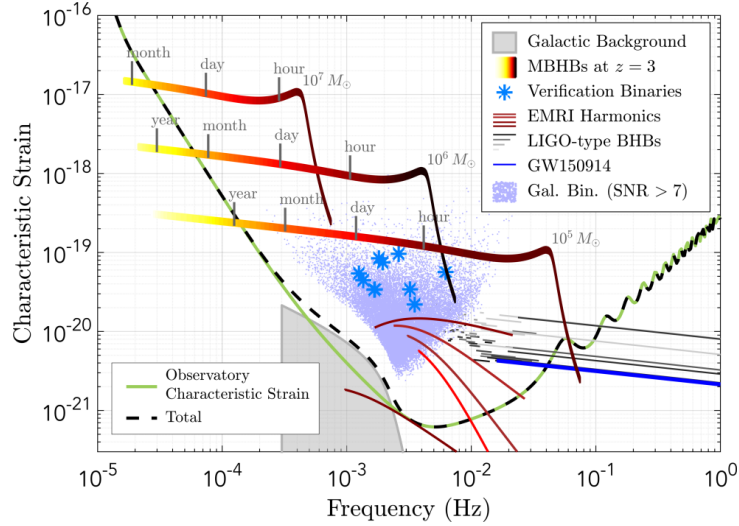


Fig. 1: GW sources in the frequency range of LISA, compared with its sensitivity for a 3-arm configuration (*credit* [7]).

EMRI GW signals are also very long, emitting around 10^5 GW cycles during the last year before plunge. Hence, GW observations of EMRIs will be a powerful tool for astrophysics, cosmology, and fundamental physics [8–13]. However, due to the complexity of EMRI GW signals, precise theoretical waveform templates are needed. They must be accurate enough to stay in phase with the emitted GWs within a detector frequency bin, and extract the system’s physical parameters from the detector data stream.

The challenge in modeling EMRIs is to compute the perturbations generated by the small body in the (background) gravitational field of the MBH, and how these perturbations affect the motion of the SCO itself. This problem is known in the literature as the *radiation reaction* problem. It is an old problem and several approaches to deal with it have been proposed (see the review by Poisson [14]). The most extended approach consists of modelling the small object using a point-like description. Then, the *radiation reaction* effects on the dynamics is described as the action of a local *self-force*, responsible for the deviations from geodesic motion. Key developments in formulating the gravitational self-force were made by Mino, Sasaki and Tanaka [15], and later, adopting an axiomatic approach, by Quinn and Wald [16]. However, these works only provide a formal description of the orbital motion. For practical calculations of the self-force, we will use the proposed *mode-sum* scheme [17–20].

To make computations without further simplifying the problem, numerical techniques ap-

pear to be a necessary tool. Numerical methods have historically been a necessity in physics in general, but especially in GR, due to the little known analytical techniques and the non-linearity of its equations. Numerical relativity [21] is therefore a growing field of study. Two different approaches are possible for the numerical implementation of the mode-sum scheme. Firstly, a frequency-domain approach, which has been used for a long time, provides accurate results for the computation of quasinormal modes and frequencies [22, 23]. On the other hand, it has more difficulties when we are interested in computing the waves that originated from highly eccentric orbits, since one has to sum over numerous modes to obtain a decent accuracy. Also, they usually solve only one point at a time.

Secondly, calculations in the time-domain can be more efficient for obtaining accurate waveforms under physically relevant situations. However, the time-domain numerical approach has to face a challenge, which consists on dealing with the different physical scales (both spatial and temporal) present in the problem, extending over several orders of magnitude. Specifically, one needs to handle not only large wavelength scales, comparable to the MBH, but also resolve scales in the vicinity of the small object, where radiation reaction effects play a crucial role. To provide the resolution that every region in the physical domain requires, a usual choice is using an adaptive scheme. Since the SCO is going to be moving through the domain (unless we choose a particular coordinate system), it is convenient to allow the adaptive scheme to change in time to properly distribute the resolution.

Our choice to deal with these issues is the “particle-without-particle” method, or PwP. It originated in previous work with the same goal, and was developed in [24–29]. The PwP method is an analytic formulation, which has been implemented previously using Finite Element Methods (FEM) [30, 31] and pseudospectral collocation methods in the time domain. Here we propose a frequency-domain implementation of the PwP technique for calculating the scalar self-force, a helpful testbed for the gravitational case. Methods in the frequency-domain are orders of magnitude faster than the ones on the time domain, and our implementation is even faster, as it computes the self-force on the whole region of interest at once, instead of point by point.

Throughout the rest of this work we use the following conventions:

- Greek letters are used to denote spacetime tensor indices.
- We use natural (geometrized) units in which $G = c = 1$.

2 EMRIs driven by a Scalar Self-Force

A simplified model for EMRIs consists on a charged scalar point-like particle orbiting a non-rotating BH. In this model, the SCO is represented as a particle, with mass m and charge q associated with a scalar field Φ . The MBH is described by a fixed spacetime geometry, in the sense that it is not affected by the charged particle. In the case of a non-rotating BH, said geometry is characterized by the Schwarzschild metric, given by the line element:

$$ds^2 = f(r) (-dt^2 + dr_*^2) + r^2 (d\theta^2 + \sin^2 \theta d\varphi^2) \quad (1)$$

With $f(r) = 1 - \frac{2M}{r}$, M the MBH mass, and

$$r_* = r + 2M \log \left| \frac{r}{2M} - 1 \right|, \quad (2)$$

the so-called *tortoise* coordinate. Given that the particle does not gravitate, the spacetime geometry is no longer dynamical. The dynamics in this case are determined by the following action:

$$\mathcal{S} [\Phi, z] = \int_{\mathcal{M}} d^4x \sqrt{-\det(g_{\alpha\beta}^{\text{BH}})} \left\{ \nabla_\mu \Phi \nabla^\mu \Phi + \int_\gamma d\tau \delta_4(x - z(\tau)) \left[\frac{m}{2} u_\mu u^\mu + q\Phi \right] \right\}, \quad (3)$$

where γ is the particle time-like worldline, with coordinates $z^\mu(\tau)$ parameterized in terms of the proper time τ . Moreover, $u = \dot{z}$ is the particle four-velocity. The first term is the scalar field's kinetic term, the one proportional to m is the standard geodesic for the particle motion, and the one proportional to q represents the coupling between field and particle motion. The latter leading to nontrivial sources in both the field equation and equation of motion.

Varying the action in Eq. (3) we derive the field equation for Φ and the equation of motion for the particle. Regarding the first, we see that the particle generates a scalar field Φ , according to the following wave-like equation (see, e.g. [14]):

$$g_{\text{BH}}^{\alpha\beta} \nabla_\alpha \nabla_\beta \Phi(x) = -4\pi q \int_\gamma d\tau \delta_4(x - z(\tau)), \quad (4)$$

where ∇_μ is the canonical connection associated with the MBH metric.

The field equation (4) has to be complemented with the equation of motion for the scalar charged particle:

$$m_* \frac{du^\mu}{d\tau} = F^\mu = q(g_{\text{BH}}^{\mu\nu} + u^\mu u^\nu) (\nabla_\nu \Phi)|_\gamma. \quad (5)$$

The coupled set of equations formed by the Partial Differential Equation (PDE) for the scalar field (4) and the Ordinary Differential Equation (ODE) for the particle trajectory (5) constitute our testbed model for an EMRI. The SCO generates a scalar field according to (4), which in turn affects the SCO motion according to (5), that is, through the action of a local force. This mechanism is analogous to the gravitational back-reaction one, which produces an inspiral via the gravitational self-force, therefore the method presented in this work can easily be extended to the gravitational case.

However, the retarded solution of (4) is singular at the particle location, whereas the force in Eq. (5) involves the gradient of the field evaluated at the particle location. Therefore, as they stand, Eqs. (4) and (5) are formal equations that require an appropriate regularization to become fully meaningful. Following [32], the retarded field can be split into two parts:

$$\Phi^{\text{ret}} = \Phi^{\text{S}} + \Phi^{\text{R}}, \quad (6)$$

a singular piece, Φ^{S} , which contains the field's singular structure and satisfies the same wave equation as the retarded field, i.e. Eq. (4); and a regular part, Φ^{R} , that satisfies the homogeneous equation associated with it. As it turns out, Φ^{R} is regular and differentiable at the particle position and is solely responsible for the scalar self-force [32]. We can therefore write the self-force experienced by the particle as:

$$F_{\text{R}}^{\mu} = q(g_{\text{BH}}^{\mu\nu} + u^{\mu}u^{\nu}) (\nabla_{\nu}\Phi^{\text{R}})|_{\gamma}, \quad (7)$$

which gives a definite sense to the equations of motion for the system.

Given that the spacetime is described by the Schwarzschild metric, which has spherical symmetry, Eq. (4) can be solved by expanding the scalar field in spherical harmonics:

$$\Phi = \sum_{\ell=0}^{\infty} \sum_{m=-\ell}^{\ell} \Phi^{\ell m}(t, r) Y^{\ell m}(\theta, \varphi). \quad (8)$$

The equation for each harmonic mode, $\Phi^{\ell m}(t, r)$, decouples from the others and satisfies a 1+1 wave equation of the form:

$$\left(-\frac{\partial^2}{\partial t^2} + \frac{\partial^2}{\partial r_*^2} - V_{\ell}(r) \right) (r\Phi^{\ell m}) = S^{\ell m} \delta(r - r_p(t)), \quad (9)$$

where $V_{\ell}(r)$ is the Regge-Wheeler potential [33] (for spin-0 fields). Its expression is:

$$V_{\ell}(r) = f(r) \left[\frac{\ell(\ell+1)}{r^2} + \frac{2M}{r^3} \right], \quad (10)$$

and the coefficient of the singular source term due to the particle presence is

$$S^{\ell m} = -\frac{4\pi q f_p}{r_p u^t} \bar{Y}^{\ell m} \left(\frac{\pi}{2}, \varphi_p(t) \right), \quad (11)$$

where $f_p = f(r_p)$, and the bar denotes complex conjugation. Here, we assume, without loss of generality, that the particle's orbit takes place in the equatorial plane: $\theta_p(t) = \pi/2$. Moreover, r_p and φ_p denote the radial and azimuthal coordinates of the particle trajectory, and they can be considered functions of the time coordinate t .

It turns out that the expansion in spherical harmonics is also useful to construct the regular field, Φ^R . Indeed, each harmonic mode of the retarded field, $\Phi_{\text{ret}}^{\ell m}(t, r)$, is actually finite and continuous at the particle location. The *sum* over ℓ is the one that diverges there. It is here where the *mode-sum* regularization scheme [17, 20, 34] comes into play, as it provides analytic expressions for the singular part of each ℓ -mode of the retarded field. These expressions are valid only near the particle location. The regularized self-force is thus obtained by numerically computing each self-force harmonic mode and subtracting the singular part provided by the mode-sum scheme. Thus, the regular part of the field gradient, $\Phi_\alpha^R \equiv \nabla_\alpha \Phi^R$, is given by

$$\Phi_\alpha^R(z^\mu(\tau)) = \lim_{x^\mu \rightarrow z^\mu(\tau)} \sum_{\ell=0}^{\infty} (\Phi_\alpha^{\text{ret}, \ell}(x^\mu) - \Phi_\alpha^{\text{s}, \ell}(x^\mu)), \quad (12)$$

where we have introduced the following notation

$$\Phi_\alpha^{\text{ret}, \ell}(x^\mu) = \sum_{m=-\ell}^{\ell} \nabla_\alpha (\Phi_{\text{ret}}^{\ell m}(t, r) Y^{\ell m}(\theta, \varphi)). \quad (13)$$

Note that each ℓ -component of the retarded field, Φ_{ret}^{ℓ} , is finite at the SCO location. From now on we will drop the *ret* sub/superscript, and refer simply to $\Phi^{\ell m}$.

We know the expression for the singular field near the SCO trajectory, which is all we need to evaluate the limit in Eq. (12). The structure of the singular field can be expressed in the following way:

$$\Phi_\alpha^{\text{s}, \ell} = q \left[\left(\ell + \frac{1}{2} \right) A_\alpha + B_\alpha + \frac{C_\alpha}{\ell + \frac{1}{2}} + \frac{D_\alpha}{(\ell - \frac{1}{2})(\ell + \frac{3}{2})} + \dots \right]. \quad (14)$$

Expressions defining the regularization parameters, A_α , B_α , C_α , and D_α , can be found in the literature for generic orbits [34–37]. Those used in this work are listed in the Appendix of [25]. These regularization parameters do not depend on ℓ , but solely on the trajectory of the particle.

The three first coefficients of (14) are responsible for the divergences, whereas the remaining terms converge to zero once they are summed over ℓ . Nevertheless high order terms like D_α can help the convergence of the numerical method.

3 The Particle-without-Particle Formulation

As we have argued before, the full retarded solution must be found numerically, and hence, it is convenient to formulate the equations in a way that we obtain smooth solutions. However, the presence of singularities in Eq. (9) makes the task difficult. To overcome this problem, the PwP formulation [24–26, 29] splits the computational domain into two disjoint regions (see Fig. 2): \mathcal{R}_- to the left of the SCO trajectory ($r < r_p(t)$) and \mathcal{R}_+ to the right ($r > r_p(t)$). Then, any non-singular quantity $Q(t, r)$ admits a decomposition

$$Q = Q^- \Theta_p^- + Q^+ \Theta_p^+, \quad (15)$$

where Θ is the Heaviside step function, $\Theta_p^- \equiv \Theta(r_p - r)$ and $\Theta_p^+ \equiv \Theta(r - r_p)$. Non-continuous quantities will have jumps across the SCO trajectory. The jump in a quantity Q will depend only on time, and is defined as:

$$[Q]_p(t) = \lim_{r \rightarrow r_p(t)} (Q^+(t, r) - Q^-(t, r)) . \quad (16)$$

For simplicity, we frequently drop the explicit dependence of the jumps in time.

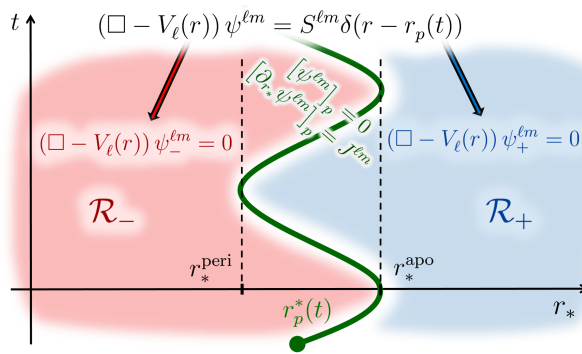


Fig. 2: Schematic representation of the PwP formulation. The field equations with singular source terms become homogeneous equations at each side of the particle worldline, together with a set of jump conditions to communicate their solutions.

Introducing:

$$r\Phi^{\ell m} = \psi^{\ell m} = \psi_-^{\ell m} \Theta_p^- + \psi_+^{\ell m} \Theta_p^+, \quad (17)$$

equation (9) transforms into two homogeneous equations without matter source terms, one at each \mathcal{R}_\pm region:

$$\left(-\frac{\partial^2}{\partial t^2} + \frac{\partial^2}{\partial r_*^2} - V_\ell(r) \right) \psi_\pm^{\ell m} = 0, \quad (18)$$

plus a set of jump conditions on $\psi_\pm^{\ell m}$ and $\partial_{r_*} \psi_\pm^{\ell m}$, which in our case read:

$$\left[\partial_{r_*} \psi^{\ell m} \right]_p = \frac{S^{\ell m}}{(1 - \dot{r}_p^{*2}) f_p} \equiv J^{\ell m}, \quad (19)$$

$$\left[\psi^{\ell m} \right]_p = 0, \quad (20)$$

where, using the geodesic equations of the SCO, $J^{\ell m}$ can be written in the following form:

$$J^{\ell m}(t) = -4\pi q \frac{r_p(t) E_p}{r_p^2(t) + L_p^2} d_{\ell m} e^{-im\varphi_p(t)}, \quad (21)$$

where E_p and L_p are the energy and orbital angular momentum of the SCO respectively (see Appendix B). Moreover, $d_{\ell m}$ is constant (after picking $\theta_p(t) = \pi/2$) and given by (see the expression of the spherical harmonics in Appendix A):

$$d_{\ell m} = \sqrt{\frac{2\ell+1}{4\pi} \frac{(\ell-m)!}{(\ell+m)!}} P_\ell^m(0). \quad (22)$$

We do not need to compute the modes with $\ell+m$ odd, given that $P_\ell^m(0) = 0$ in that case. From Eq. (21) it follows that all the time dependence in $J^{\ell m}$ comes from the radial dependence in the amplitude and the azimuthal dependence in the phase. Regarding the azimuthal dependence, and following the discussion in Appendix B, the evolution of the azimuthal angle $\varphi_p(t)$ of the SCO trajectory has two parts: (i) A secular piece that evolves linearly in time, $\omega_\varphi t$, with ω_φ the azimuthal angular frequency (time that takes to cover an angle of 2π around the z axis; see Appendix B); (ii) A piece that oscillates with the radial period T_r (time to go from periapsis to apoapsis and back) that we call $\Delta\varphi_p(t)$ [see Eq. (106)]. This analysis of the time structure of $J^{\ell m}$ is going to be relevant for frequency-domain analysis later in Sec. 4.

In order to have a well-posed initial-value problem, we need to add boundary conditions. In this case, the boundary conditions have to be prescribed both at the event horizon ($r_* \rightarrow -\infty$) and at spatial infinity ($r_* \rightarrow +\infty$). At both extremes the field has to be purely outgoing

(with respect to the integration direction), in other words, the field can only be ingoing at the horizon and outgoing at spatial infinity.

$$(\partial_t \pm \partial_{r_*}) \psi_{\pm}^{\ell m} \Big|_{r_* \rightarrow \pm\infty} = 0, \quad (23)$$

In summary, at each region, we have equations without the singular terms induced by the SCO. Then, since these equations are strongly hyperbolic we obtain smooth solutions. Finally, the SCO appears in the communication between the two regions by enforcing the jump conditions. The spherical symmetry of the MBH background leads to jumps only in the time and radial derivatives of the metric perturbations, which are not independent. In particular, for first-order derivatives we find:

$$[\partial_t Q^{\ell m}]_p = \frac{d}{dt} [Q^{\ell m}]_p - \dot{r}_p^* [\partial_r Q^{\ell m}]_p, \quad (24)$$

and similarly for derivatives of higher order. Then,

$$[\partial_t \psi^{\ell m}]_p = -\frac{\dot{r}_p^* S^{\ell m}}{(1 - \dot{r}_p^{*2}) f_p}, \quad (25)$$

4 PwP in the Frequency Domain

We decide to use a frequency-domain approach for its speed, as it is orders of magnitude less computationally intensive than to time domain methods. To do so, we consider the Fourier transform of the components at each side of the particle, i.e. $\psi_{\pm}^{\ell m}(t, r)$, instead of the full solution $\psi^{\ell m}(t, r)$, which is not smooth due to the particle's presence. They are defined as:

$$\tilde{\psi}_{\pm}^{\ell m}(\omega, r) = \frac{1}{\sqrt{2\pi}} \int_{-\infty}^{+\infty} dt e^{-i\omega t} \psi_{\pm}^{\ell m}(t, r), \quad (26)$$

with inverse

$$\psi_{\pm}^{\ell m}(t, r) = \frac{1}{\sqrt{2\pi}} \int_{-\infty}^{+\infty} d\omega e^{i\omega t} \tilde{\psi}_{\pm}^{\ell m}(\omega, r). \quad (27)$$

The jump at the particle location $J^{\ell m}$, Eq. (21), together with Eq. (106) in Appendix B, can now be written as:

$$J^{\ell m}(t) = -4\pi q \frac{r_p(t) E_p}{r_p^2(t) + L_p^2} d_{\ell m} e^{-im\Delta\varphi_p(t)} e^{-im\omega_{\varphi} t}. \quad (28)$$

It is crucial to take into account that we are considering only bounded trajectories of the SCO around the MBH, i.e. circular or eccentric trajectories. As a consequence, $J^{\ell m}$ has a special

time structure. We can see from Eq. (28), that the last factor oscillates with a single frequency, a multiple of the azimuthal frequency, whereas the rest is a function of the radial motion only. This second factor oscillates with a number of frequencies that are multiples of the radial frequency ω_r . The conclusion is that the jump $J^{\ell m}$ can be expanded as a discrete Fourier series of the form:

$$\left[\partial_{r_*} \psi^{\ell m} \right]_p(t) = J^{\ell m}(t) = \sum_{n=-\infty}^{n=+\infty} J_{\ell mn} e^{-i\omega_{mn}t}, \quad (29)$$

where the frequencies ω_{mn} do not depend on ℓ :

$$\omega_{\ell mn} = n\omega_r + m\omega_\varphi \equiv \omega_{mn}. \quad (30)$$

We just need to sum over n because the only dependence of the jump on the azimuthal frequency ω_φ comes from the scalar spherical harmonics [see Eqs. (19), (20), and (11)]. The coefficients $J_{\ell mn}$ of the Fourier series can be obtained from

$$J_{\ell mn} = \frac{1}{T_r} \int_0^{T_r} dt J^{\ell m}(t) e^{i\omega_{mn}t} = -\frac{4\pi q E_p}{T_r} d_{\ell m} \int_0^{T_r} dt \frac{r_p(t)}{r_p^2(t) + L_p^2} e^{in\omega_r t} e^{im(\omega_\varphi t - \varphi_p(t))}. \quad (31)$$

The discrete structure of the jumps, Eq. (29), together with the boundary conditions, implies that also the scalar field variable at both sides of the SCO can be expressed in terms of a discrete Fourier series:

$$\psi_\pm^{\ell m}(t, r) = \sum_{n=-\infty}^{+\infty} e^{-i\omega_{mn}t} R_{\ell mn}^\pm(r), \quad (32)$$

$$= e^{-im\omega_\varphi t} \sum_{n=-\infty}^{+\infty} e^{-in\omega_r t} R_{\ell mn}^\pm(r), \quad (33)$$

where the coefficients of the series, $R_{\ell mn}^\pm(r)$, only depend on the radial coordinate and hence they satisfy ODEs. By introducing Eq. (33) into the wave equations in Eq. (18), we obtain a time-independent Schrödinger-type equation, satisfied by the $R_{\ell mn}^\pm$ coefficients:

$$\left(\frac{d^2}{dr_*^2} - V_\ell(r) + \omega_{nm}^2 \right) R_{\ell mn}^\pm = 0. \quad (34)$$

In order to solve these ODEs (for each (ℓ, m, n)) we need two boundary conditions for each, since they are 2nd-order equations. The first pair comes from the ingoing and outgoing conditions at spatial infinity and at the horizon [Eq. (23)]. They become the following conditions on the radial functions $R_{\ell mn}$:

$$\left(i\omega_{mn} \mp \frac{d}{dr_*} \right) R_{\ell mn}^\pm \Big|_{r_* \rightarrow \pm\infty} = 0. \quad (35)$$

The second pair is the junction condition for the radial functions $R_{\ell nm}^\pm$, which are given by [from Eqs. (19), (20), and (29)]

$$\sum_{n=-\infty}^{+\infty} e^{-in\omega_r t} [R_{\ell mn}]_p = 0, \quad (36)$$

$$e^{-im\omega_\phi t} \sum_{n=-\infty}^{+\infty} e^{-in\omega_r t} \left[\frac{dR_{\ell mn}}{dr_*} \right]_p = J^{\ell m}. \quad (37)$$

In the case of circular orbits ($r_p(t) = \text{const.}$) we have both $R_{\ell mn}^\pm(r_p)$ and $J^{\ell m}$ constant. This means that the only non-zero coefficient is the $n = 0$. Therefore, for circular orbits, the conditions in Eqs. (36) and (37) reduce to

$$[R_{\ell m0}]_p = 0, \quad (38)$$

$$\left[\frac{dR_{\ell m0}}{dr_*} \right]_p = J_{\ell m0}, \quad (39)$$

where the coefficients $J_{\ell mn}$, which are determined from Eq. (19), are the Fourier components of the jump in the scalar field's gradient at the particle location.

4.1 Grid Structure for the Numerical Computations

The PwP method is based on a domain splitting defined in terms of the tortoise coordinate:

$$r_* \in (-\infty, \infty) = \left(-\infty, r_p^*(t) \right) \cup \left(r_p^*(t), +\infty \right), \quad (40)$$

We are implicitly assuming that the evolution progresses following a $\{t = \text{const.}\}$ spacetime slicing. Each slice goes from the event horizon to spatial infinity. With this assumption, we need to decide whether we construct the numerical grid by truncating the physical domain or, instead, use a different coordinate system, in which we cover the horizon and spatial infinity in a finite coordinate range. The first option is by far the most commonly used, but it has a drawback. If we keep the same boundary conditions [Eq. (23)], we are going to accumulate an error since these boundary conditions are not exact when applied to a finite value of r_* and reflections of the field will occur. In a time-domain computation, we can set the location of the *truncated* boundaries in such a way that they always remain out of causal contact with the particle. Thus, avoiding any contamination from the boundaries to the solution around the particle. However, when working in the frequency domain we are solving elliptic ODEs, whose solution is fully determined by the conditions we prescribe at the boundaries.

There are two possible ways to proceed: (i) To obtain precise boundary conditions, expanding our equations near the horizon and near spatial infinity (see [38]). (ii) To use a new coordinate system in which the horizon and spatial infinity are located at finite values of the new coordinates (S_- and S_+), so that the boundary conditions are still valid.

Here, we choose the second option. The naive approach would be to compactify just the radial coordinate. While this would solve the problem in the boundary conditions, it would create another problem, namely that many radiation cycles would accumulate near the boundaries, making it impossible to resolve them appropriately. Instead, we use a hyperboloidal compactification [39], where we also change the time coordinate (the slicing of the spacetime in $t = \text{const.}$ hypersurfaces). With this slicing, we will only have a few cycles, in such a way that they can be resolved numerically. In particular, we essentially follow the method in [39], with a multi-domain splitting of our computational grid so that the hyperboloidal compactification is applied only to suitable boundary regions (extending from a certain point to the event horizon and spatial infinity respectively).

Following these ideas, we use a multi-domain method with the following characteristics (see Fig. 3): We have in total six domains, three from the horizon to the apocenter and three from the pericenter to spatial infinity. That is, we have:

$$\mathcal{R}_- = [S_-, \rho_T^-] \cup [\rho_T^-, R_-] \cup [R_-, r_{\text{apo}}^*] , \quad (41)$$

$$\mathcal{R}_+ = [r_{\text{peri}}^*, R_+] \cup [R_+, \rho_T^+] \cup [\rho_T^+, S_+] . \quad (42)$$

Here, $[R_-, r_{\text{apo}}^*]$ and $[r_{\text{peri}}^*, R_+]$ are regular domains in the sense that they are based on the tortoise coordinate and therefore, the equations are unchanged. At the domains $[S_-, \rho_T^-]$ and $[\rho_T^+, S_+]$ we use the hyperboloidal compactification described below, with a new radial coordinate, ρ . Finally, $[\rho_T^-, R_-]$ and $[R_+, \rho_T^+]$ are transition domains, convenient for numerical purposes. With this setup, we break the problem of finding the frequency-domain modes into two problems (one for each mode). It is important to remark that we are going to use overlapping domains:

$$\mathcal{R}_- \cap \mathcal{R}_+ = [r_{\text{peri}}^*, r_{\text{apo}}^*] . \quad (43)$$

This, as we explain later, is a crucial feature when implementing the frequency-domain computations. In the case of circular orbits, the intersection reduces to a point, the orbit.

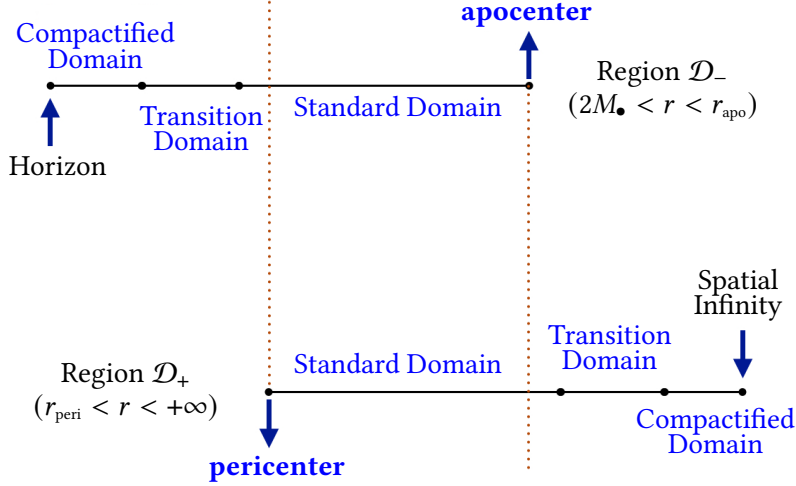


Fig. 3: Schematic representation of the structure of the domains used in the frequency-domain solution of the scalar field equations.

4.2 Hyperboloidal Compactification in Schwarzschild Spacetime

The idea of the hyperboloidal compactification is not only to compactify the radial coordinate, but also to change the character of the foliation so that it approaches future null infinity to the right of the SCO and the BH horizon to the left (see Fig. 4). The reason for this is that compactifying the radial coordinate alone, without changing the slicing (changing the time coordinate), is known to introduce resolution problems in the numerical implementation [40, 41] whereas no resolution problems appear in hyperboloidal coordinates [39].

The change of slicing we use for the hyperboloidal compactification is given by the transformation: $(t, r_*) \rightarrow (\tau, \rho)$ with

$$\tau = \begin{cases} t + h^-(r_*), & \text{if } r_* < R_- \\ t - h^+(r_*), & \text{if } r_* > R_+, \end{cases} \quad (44)$$

and

$$r_*(\rho) = \begin{cases} \rho/\Omega_-(\rho), & \text{if } \rho < R_- \\ \rho/\Omega_+(\rho), & \text{if } \rho > R_+. \end{cases} \quad (45)$$

The functions $h^\pm(r_*)$ are chosen in such a way that the change of slicing preserves the radial null ingoing/outgoing geodesics (characteristics):

$$t \mp r_* = \tau \mp \rho. \quad (46)$$

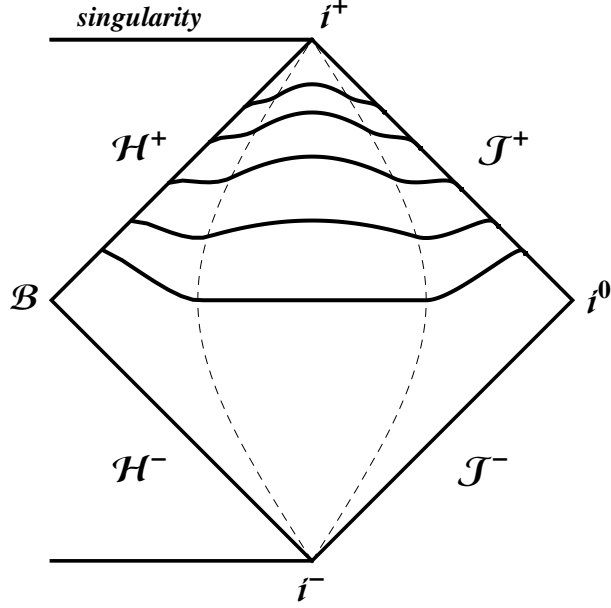


Fig. 4: Penrose-Carter diagram of the hyperboloidal compactification.

This implies the following relationship:

$$\rho = r_* - h^\pm(r_*). \quad (47)$$

On the other hand, from Eq. (45), the Jacobian of r_* and ρ is given by:

$$\frac{d\rho}{dr_*} = \frac{\Omega_\pm^2}{\Omega_\pm - \rho\Omega'_\pm}, \quad \Omega'_\pm \equiv \frac{d\Omega_\pm}{d\rho}. \quad (48)$$

The condition in Eq. (46) solves the resolution problem of compactification, since the relation of ρ to τ along outgoing null rays is the same as the relation of r_* to t , so when the solution is essentially outgoing one can compactify without running into resolution problems. Moreover, the representation of the timelike Killing vector in the Schwarzschild metric is left invariant, that is: $\partial/\partial t = \partial/\partial \tau$. This ensures that the components of the Schwarzschild metric in the (τ, ρ) coordinates are time independent.

The radial coordinate ρ introduced in Eq. (45) is the coordinate compactifying the radial direction and is chosen so that $r_* \rightarrow +\infty$ corresponds to $\rho = S_+$ and $r_* \rightarrow -\infty$ ($r = 2M$) corresponds to $\rho = S_-$, both being finite. The coordinates r_* and ρ agree at the interfaces R_\pm . The change of slicing of Eq. (44), together with the compactification, implies that S_+ corresponds to a sphere at future null infinity, and S_- corresponds to a sphere at the MBH horizon. The specific relation between ρ and r_* is determined by the form of the functions

$\Omega_{\pm}(\rho)$. In this work, we choose a smooth transition [42] via:

$$\Omega_{\pm}(\rho) = 1 - F(\rho) \frac{\rho}{S_{\pm}}, \quad (49)$$

where $F(\rho)$ is a smooth function going from 0 to 1 at each hyperboloidal layer. The choice of transition function, adapted to the domain decomposition of Eqs. (41) and (42) is:

$$F(\rho) = \begin{cases} 1, & \text{if } S_- \leq \rho < \rho_T^- \\ F_T(\sigma(\rho; R_-, \rho_T^-)), & \text{if } \rho_T^- \leq \rho < R_- \\ 0, & \text{if } R_- < \rho < R_+ \\ F_T(\sigma(\rho; R_+, \rho_T^+)), & \text{if } R_+ \leq \rho < \rho_T^+ \\ 1, & \text{if } \rho_T^+ < \rho \leq S_+, \end{cases} \quad (50)$$

where σ is a function of three arguments, linear in ρ

$$\sigma(\rho; \rho_i, \rho_f) = \frac{\pi}{2} \frac{\rho - \rho_i}{\rho_f - \rho_i}, \quad (51)$$

and F_T is a function of σ given by [43]

$$F_T(\sigma) = \frac{1}{2} \left\{ 1 + \tanh \left[\frac{s}{\pi} \left(\tan \sigma - \frac{q^2}{\tan \sigma} \right) \right] \right\}. \quad (52)$$

The free parameter q , determines the point $\rho = \rho_{1/2}$, where $F_T = 1/2$, and s determines the slope of F_T at $\rho = \rho_{1/2}$. The Jacobians of the derivative operators from (t, r_*) to (τ, ρ) read

$$\frac{\partial}{\partial t} = \frac{\partial}{\partial \tau}, \quad \frac{\partial}{\partial r_*} = -H \frac{\partial}{\partial \tau} + (1 - H) \frac{\partial}{\partial \rho}. \quad (53)$$

Here, the function H is defined as follows:

$$H \equiv \frac{dh^{\pm}}{dr_*}. \quad (54)$$

And, using the relation in Eq. (47), it can also be written in the following form:

$$H = 1 - \frac{d\rho}{dr_*} = 1 - \frac{\Omega_{\pm}^2}{L_{\pm}}, \quad (55)$$

where

$$L_{\pm} = \Omega_{\pm} - \rho \frac{d\Omega_{\pm}}{d\rho} = \Omega_{\pm} - \rho \Omega'_{\pm}. \quad (56)$$

Some interesting expressions regarding the hyperboloidal compactification can be found in Appendix C. In the hyperboloidal slices (i.e. in subdomains $[S_-, \rho_T^-]$, $[\rho_T^-, R_-]$, $[R_+, \rho_T^+]$, and $[\rho_T^+, S_+]$; see Fig. 3) we define a second scalar field variable:

$$\varphi^{\ell m} \equiv \partial_{\rho} \psi^{\ell m}. \quad (57)$$

Then, in the coordinates of the hyperboloidal compactification, we can introduce analogous Fourier expansions for $\psi^{\ell m}$ and $\varphi^{\ell m}$:

$$\psi_{\pm}^{\ell m}(\tau, \rho) = e^{-im\omega_{\varphi}\tau} \sum_{n=-\infty}^{+\infty} e^{-in\omega_r\tau} R_{\ell mn}^{\pm}(\rho), \quad (58)$$

$$\varphi_{\pm}^{\ell m}(\tau, \rho) = e^{-im\omega_{\varphi}\tau} \sum_{n=-\infty}^{+\infty} e^{-in\omega_r\tau} Q_{\ell mn}^{\pm}(\rho), \quad (59)$$

so that we can derive the following first-order ODEs for $(R_{\ell mn}^{\pm}, Q_{\ell mn}^{\pm})$:

$$\frac{dR_{\ell mn}^{\pm}}{d\rho} = Q_{\ell mn}^{\pm}, \quad (60)$$

$$\left[\frac{1 - H_{\pm}}{1 + H_{\pm}} \frac{d}{d\rho} \mp \frac{2i\omega_{mn}H_{\pm}}{1 + H_{\pm}} - \frac{H'_{\pm}}{1 + H_{\pm}} \right] Q_{\ell mn}^{\pm} + \left[\omega_{mn}^2 \mp \frac{i\omega_{mn}H'_{\pm}}{1 + H_{\pm}} - \frac{V_{\ell}}{1 - H_{\pm}^2} \right] R_{\ell mn}^{\pm} = 0. \quad (61)$$

These equations are equivalent to Eq. (34) in the limit $H_{\pm} \rightarrow 0$. We can also reduce Eq. (34) to first-order ODEs just by introducing variables $Q_{\ell mn}^{\pm}$ in the same way as in Eq. (60), that is:

$$Q_{\ell mn}^{\pm} = \frac{dR_{\ell mn}^{\pm}}{dr_*}. \quad (62)$$

The hyperboloidal compactification allows us to impose exact boundary conditions since we are including in our computational domain both the horizon and spatial infinity. The exact boundary conditions can be derived directly from Eqs. (63) and (64). In the frequency domain, the boundary condition at the horizon is:

$$i\omega_{mn}R_{\ell mn}^{-} + Q_{\ell mn}^{-} = 0, \quad (63)$$

and at spatial infinity:

$$-i\omega_{mn}R_{\ell mn}^{+} + Q_{\ell mn}^{+} = 0. \quad (64)$$

4.3 Method of Extended Homogeneous Solutions

In the frequency-domain, the ℓm -harmonics of the scalar self-force on bounded geodesics are found by decomposing the retarded field in a Fourier series with indices (ℓ, m, n) . The main advantage is that the computation involves only ODEs. The drawback is that it was found that for the case of eccentric orbits the sum over n has bad convergence properties. In [38], a solution to this problem was proposed. The key point of the method is to use the homogeneous solutions to construct the modes of the self-force instead of the inhomogeneous ones, and

hence the method was named method of *extended homogeneous solutions*. The method leads to exponential convergence to the value of the self-force ℓm -modes. Our implementation of the frequency-domain solver for the self-force modes is similar to the method of extended homogeneous solutions of [38]. The reason for this is that the PwP already works with homogeneous solutions, since it eliminates the explicit presence of the particle in the equations, by moving it to the boundary conditions across the interface between two domains. The method is designed in such a way that the particle is always located at the interface, even for eccentric orbits.

In the first place, we should solve the scalar field equations in the two regions \mathcal{R}_\pm . The equations we need to consider are Eqs. (60) and (61) in the compactified and transition domains (see Fig. 3) and Eq. (34) in the regular domains. These equations have to be complemented with boundary conditions in order to have a unique solution. The boundary conditions at the horizon and at spatial infinity are now clear after adopting the hyperboloidal compactification [Eqs. (63) and (64) respectively]. These conditions are actually automatically satisfied, given that our slices become null both at the horizon and at spatial infinity.

It remains to prescribe boundary conditions at the pericenter and apocenter. But we only have the information from the jumps in the scalar field due to the presence of the SCO [Eqs. (36) and (37)], so it is not clear how this can be done. The idea to extend the domain \mathcal{R}_- up to the apocenter and the domain \mathcal{R}_+ up to the pericenter is to have in both domains the whole (radial) trajectory of the SCO. We then compute the self-force at all the trajectory points, by solving the scalar field equations just once, thanks to the field equations being linear.

Therefore, we can prescribe arbitrary Dirichlet-type boundary conditions at pericenter and apocenter, and afterwards rescale the solutions (multiply by an arbitrary factor) so that the jump conditions [Eqs. (36) and (37)] are satisfied. Of course, the multiplicative factor will be different at \mathcal{R}_- and \mathcal{R}_+ , and in addition, it will be different for each point in the radial interval $[r_{\text{peri}}^*, r_{\text{apo}}^*]$. Given that the solutions that we find by prescribing arbitrary boundary conditions at pericenter and apocenter are not the ones from which we are going to do the physical computations we will refer to them by using a hat: $(\hat{R}_{\ell mn}^\pm, \hat{Q}_{\ell mn}^\pm)$. Then, following this

argument, we prescribe the following boundary conditions:

$$\hat{R}_{\ell mn}^-(r_{\text{apo}}) = \lambda^-, \quad (65)$$

$$\hat{R}_{\ell mn}^+(r_{\text{peri}}) = \lambda^+, \quad (66)$$

where $\lambda^\pm \in \mathbb{C}$. We choose them as follows: $\Re(\lambda^+) = \Re(\lambda^-) = 1$.

Now the question is how, from the solutions $(\hat{R}_{\ell mn}^\pm, \hat{Q}_{\ell mn}^\pm)$, can we find the solutions that we are actually interested in (taking into account the presence of the particle). Here is where the linearity of our equations becomes useful. Given a point in the SCO trajectory, $\hat{r}_p = r_p(\hat{t})$ (for a certain arbitrary time \hat{t}), the true solution, the one satisfying the jump conditions, is going to be given by

$$R_{\ell mn}(r) = \begin{cases} C_{\ell mn}^- \hat{R}_{\ell mn}^-(r), & \text{if } r \leq \hat{r}_p, \\ C_{\ell mn}^+ \hat{R}_{\ell mn}^+(r), & \text{if } r \geq \hat{r}_p. \end{cases} \quad (67)$$

where the coefficients $C_{\ell mn}^\pm$ are constants (depending on the location of the SCO) to be determined uniquely by enforcing the jump conditions (36) and (37). This expression is valid for any \hat{r}_p . Moreover, taking into account that $Q_{\ell mn}$ is simply the derivative of $R_{\ell mn}$, we have an analogous expression for $Q_{\ell mn}$. The jumps that appear, when evaluated at a particular location \hat{r}_p , have the following expression:

$$[R_{\ell mn}]_p = C_{\ell mn}^+ \hat{R}_{\ell mn}^+ - C_{\ell mn}^- \hat{R}_{\ell mn}^-, \quad (68)$$

$$[Q_{\ell mn}]_p = C_{\ell mn}^+ \hat{Q}_{\ell mn}^+ - C_{\ell mn}^- \hat{Q}_{\ell mn}^-. \quad (69)$$

Given that Eqs. (36) and (37) have to be satisfied independently of the time corresponding to the particular location \hat{r}_p , the obvious option is that those equations are satisfied for each Fourier mode, that is, for each n . Then, we impose

$$C_{\ell mn}^+ \hat{Q}_{\ell mn}^+(\hat{r}_p) - C_{\ell mn}^- \hat{Q}_{\ell mn}^-(\hat{r}_p) = J_{\ell mn}, \quad (70)$$

$$C_{\ell mn}^+ \hat{R}_{\ell mn}^+(\hat{r}_p) - C_{\ell mn}^- \hat{R}_{\ell mn}^-(\hat{r}_p) = 0, \quad (71)$$

for each value of n . So the coefficients $C_{\ell mn}^\pm$ are:

$$C_{\ell mn}^- = \frac{\hat{R}_{\ell mn}^+(\hat{r}_p)}{W[\hat{R}_{\ell mn}^-, \hat{R}_{\ell mn}^+](\hat{r}_p)} J_{\ell mn}, \quad (72)$$

$$C_{\ell mn}^+ = \frac{\hat{R}_{\ell mn}^-(\hat{r}_p)}{W[\hat{R}_{\ell mn}^-, \hat{R}_{\ell mn}^+](\hat{r}_p)} J_{\ell mn}. \quad (73)$$

The denominator of these expressions corresponds to the Wronskian of the ordinary differential equations for $R_{\ell mn}^\pm$, that is:

$$W[\hat{R}_{\ell mn}^-, \hat{R}_{\ell mn}^+] = \hat{R}_{\ell mn}^- \frac{d\hat{R}_{\ell mn}^+}{dr_*} - \hat{R}_{\ell mn}^+ \frac{d\hat{R}_{\ell mn}^-}{dr_*} \quad (74)$$

$$= \hat{R}_{\ell mn}^- \hat{Q}_{\ell mn}^+ - \hat{R}_{\ell mn}^+ \hat{Q}_{\ell mn}^- . \quad (75)$$

We can then substitute Eqs. (72) and (73) into Eq. (67) to have a solution for $R_{\ell mn}(r)$ (or for $R_{\ell mn}^+(r)$ and $R_{\ell mn}^-(r)$) that all together satisfy the jump conditions.

4.4 Numerical implementation

Up till now, we have presented an analytic approach to the computation of the scalar self-force using the PwP method in the frequency domain. Given that the differential equations involved do not seem to admit analytic solutions, we need to resort to numerical computations. The goal of this project is to solve numerically the ODEs given by Eqs. (60) and (61).

The original equations can be written in an ODE form as follows:

At the horizon region we have

$$\begin{aligned} \frac{dR_{\ell mn}^-}{d\rho} &= Q_{\ell mn}^- \\ \frac{dQ_{\ell mn}^-}{d\rho} &= \frac{\frac{dH^-}{d\rho}}{1-H^-} (Q_{\ell mn}^- + i\omega_{mn}R_{\ell mn}^-) + \frac{2i\omega_{mn}H^-}{1-H^-} Q_{\ell mn}^- \\ &\quad - \left(\frac{1+H^-}{1-H^-} \omega_{mn}^2 - \frac{V_\ell}{(1-H^-)^2} \right) R_{\ell mn}^- , \end{aligned} \quad (76)$$

and at the Infinity region

$$\begin{aligned} \frac{dR_{\ell mn}^+}{d\rho} &= Q_{\ell mn}^+ \\ \frac{dQ_{\ell mn}^+}{d\rho} &= \frac{\frac{dH^+}{d\rho}}{1-H^+} (Q_{\ell mn}^+ - i\omega_{mn}R_{\ell mn}^+) - \frac{2i\omega_{mn}H^+}{1-H^+} Q_{\ell mn}^+ \\ &\quad - \left(\frac{1+H^+}{1-H^+} \omega_{mn}^2 - \frac{V_\ell}{(1-H^+)^2} \right) R_{\ell mn}^+ , \end{aligned} \quad (77)$$

In order to implement numerically the ODEs we separate the real and imaginary parts:

$$R_{\ell mn}^\pm = R_{\ell mn}^{r\pm} + iR_{\ell mn}^{i\pm} , \quad (78)$$

$$Q_{\ell mn}^\pm = Q_{\ell mn}^{r\pm} + iQ_{\ell mn}^{i\pm} , \quad (79)$$

where the superscripts have the following meaning: 'r' real part, 'i' imaginary part, '+' infinity region, '-' horizon region.

The integration of these ODEs goes as follows. At the horizon region, we integrate Eqs. (76) from $\rho = S_-$ to $\rho_{\text{apo}} = r_{\text{apo}}$. And at the Infinity region we should integrate Eqs. (77) from $\rho = S_+$ to $\rho_{\text{peri}} = r_{\text{peri}}$. This requires imposing *initial conditions* for $(R_{\ell mn}^-, Q_{\ell mn}^-)$ at $\rho = S_-$, and for $(R_{\ell mn}^+, Q_{\ell mn}^+)$ at $\rho = S_+$. Taking into account the ingoing/outgoing boundary conditions (63) and (64), the initial conditions can be taken as follows. At the horizon

$$R_{\ell mn}^-(S_-) = 1, \quad Q_{\ell mn}^-(S_-) = -i\omega_{mn}R_{\ell mn}^-(S_-) = -i\omega_{mn}. \quad (80)$$

and at Infinity

$$R_{\ell mn}^+(S_+) = 1, \quad Q_{\ell mn}^+(S_+) = i\omega_{mn}R_{\ell mn}^+(S_+) = i\omega_{mn}. \quad (81)$$

without any arbitrary constants, given that we are going to use conditions (65) and (66).

There are several things that need to be taken care of. First, the behaviour near the extremes presents special behavior in such a way that integrating the ODEs from these points may induce instabilities and/or inaccuracies in the solution. Secondly, note that the Regge-Wheeler potential, Eq. (10), is actually flat at the horizon, but is dominated by the $\ell(\ell+1)$ term far from it, and decreases slowly. This leads to the following behaviour for $R_{\ell 00}^+$ near infinity:

$$R_{\ell 00}^+(\rho) \xrightarrow{\varepsilon \rightarrow 0} \varepsilon^\ell \{ \Sigma_0 + \Sigma_1 \varepsilon + \Sigma_2 \varepsilon^2 + \dots \} \quad \text{with} \quad \varepsilon = S_+ - \rho. \quad (82)$$

Then, in practice, we begin integrating at $\rho_H^+ \equiv S_- + \varepsilon_H$, and $\rho_I^- \equiv S_+ - \varepsilon_I$, to avoid the divergences at both the horizon and spatial infinity. Also, ε_I will need to be larger for the $(\ell, 0, 0)$ modes, otherwise, the numerical method may become unstable.

Once we have the values for $R_{\ell mn}^\pm$ and $Q_{\ell mn}^\pm$ we can finally obtain the self-force caused by the ℓ -components of the retarded field [Eq. (13)]:

$$\Phi_\alpha^\ell(x^\mu) = \sum_{m=-\ell}^{\ell} \nabla_\alpha (\Phi^{\ell m}(t, r) Y^{\ell m}(\theta, \varphi)) \equiv \frac{F_\mu^\ell}{q}. \quad (83)$$

Then,

$$F_\mu^\ell = q \sum_{m=-\ell}^{\ell} (\nabla_\alpha \Phi^{\ell m}) Y^{\ell m} + \Phi^{\ell m} \nabla_\alpha Y^{\ell m}, \quad (84)$$

and we can compute the t , r and φ components; taking into account that $\Phi^{\ell m} = \psi^{\ell m}/r$:

$$F_t^\ell = \frac{q}{r_p} \sum_{m=-\ell}^{\ell} (\partial_t \psi^{\ell m}) Y^{\ell m} \quad (85)$$

$$F_r^\ell = \frac{q}{r_p} \sum_{m=-\ell}^{\ell} \left(\partial_r - \frac{1}{r} \right) \psi^{\ell m} Y^{\ell m} \quad (86)$$

$$F_\varphi^\ell = \frac{q}{r_p} \sum_{m=-\ell}^{\ell} i m \psi^{\ell m} Y^{\ell m} \quad (87)$$

With all the expressions being evaluated at the particle worldline γ . Introducing the expansion of $\psi^{\ell m}$ in Fourier modes according to Eq. (33), and omitting the \pm signs, we obtain the *retarded* self-force at the particle location:

$$F_t^\ell = \frac{q}{r_p} \sum_{m,n} (-i\omega_{mn} d_{\ell m}) R_{\ell mn} e^{i(m\varphi_p - \omega_{mn} t_p)} e^{-i\omega_r t_p} \quad (88)$$

$$F_r^\ell = \frac{q}{r_p} \sum_{m,n} d_{\ell m} \left(\frac{Q_{\ell mn}}{f_p} - \frac{R_{\ell mn}}{r_p} \right) e^{i(m\varphi_p - \omega_{mn} t_p)} \quad (89)$$

$$F_\varphi^\ell = \frac{q}{r_p} \sum_{m,n} (i m d_{\ell m}) R_{\ell mn} e^{i(m\varphi_p - \omega_{mn} t_p)} \quad (90)$$

We can then obtain the *regular* self-force subtracting the singular part [Eq. (12)].

5 Code implementation

We have developed a software from scratch that computes the self-force according to the explained scheme. It can be found publicly on Github (<https://github.com/Pastells/TFM>). The main program is coded in Python (3.8.5), while the ODE solver we use is from Julia (1.6.1).

In the code we refer to $[S_-, r_{\text{peri}}^*]$ as the Horizon Domain (HD), and to $[r_{\text{apo}}^*, S_+]$ as the Infinity Domain (ID). Then $[r_{\text{peri}}^*, r_{\text{apo}}^*]$ is the Orbital Domain (OD), also HOD or IOD when referred from an integration viewpoint coming from either the HD or the ID.

5.1 Code structure

The project is structured in several files as follows (see Fig. 5):

- `self_force.py` is the main program, with loops for computing the (l, m, n) modes, computation of the singular part of the self-force, Eq. (14), to subtract it from the retarded part (the one computed in the loops), and obtain the *regular self-force*. We limit the maximum number of ℓ modes from the start, as an input for the program. Only $m \geq 0$ are computed, given the relation in Appendix A; and enough n modes are used to achieve convergence, going at most from $-N_{\text{Fourier}}$ to $+N_{\text{Fourier}}$.
- `mode_comp.jl`. Main Julia file, where the ODEs are solved. It contains a function for solving the equations at all 4 different domains (HD, HOD, ID, IOD), as well as a function for the V_ℓ potential [Eq. (10)].
- `class_SF_Physics.py` defines the class `Physical_Quantities`, which has all the physical variables and arrays to contain intermediate and final results, as well as related functions.
- `Schwarzschild.py` contains functions related to the Schwarzschild metric, as one used to obtain the r coordinate from the tortoise coordinate.
- `orbital_computation.py`. Functions for the particle motion (see Appendix B). Obtains the trajectory and all points where the self-force is evaluated.
- `compactification.jl`. Functions for hyperboloidal compactification (Sec. 4.2).
- `utils.py`. Some useful functions, like the ones for computing the spectral coefficients and value of the jump [Eq. (31)], and setting up a logger via the logging package.

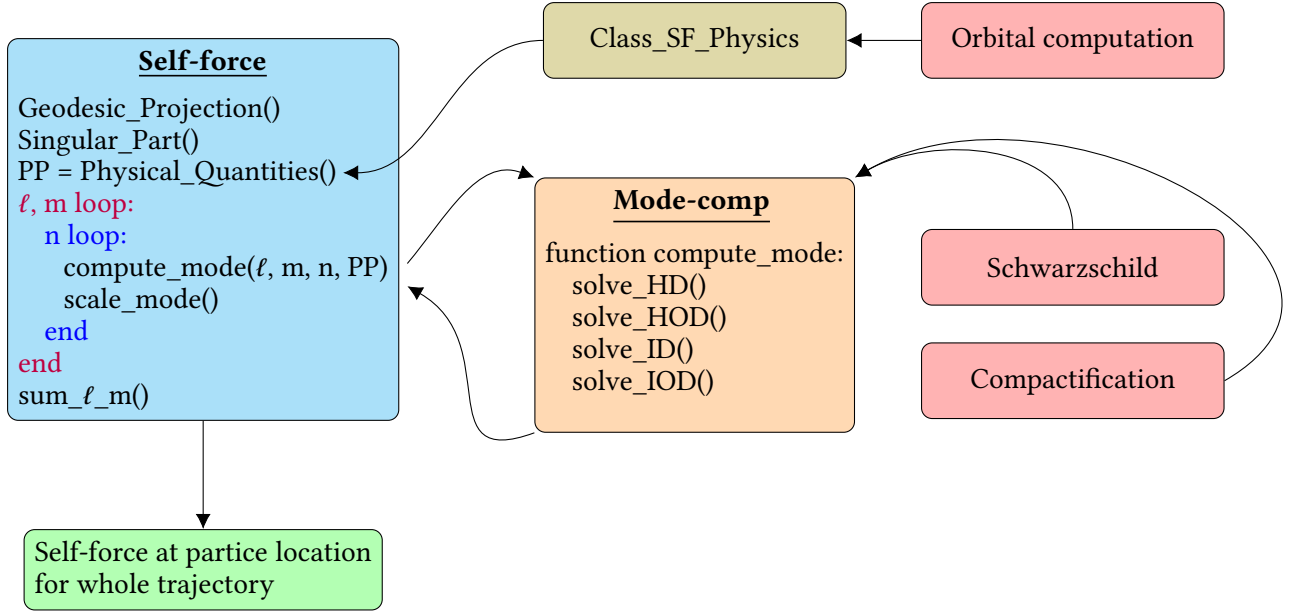


Fig. 5: Schematic structure of the software project. Each node represents a different file, with the objects ending in brackets being functions, while the arrows show the dependencies of each file. Note that we do not show the utils file, used in both “Self-force” and “class_SF_Physics”.

Furthermore, a CSV file with the simulation parameters is needed as input for the program. It contains the following parameters (with the defaults used shown as an equality):

- $\text{Max_ell} = 20$. Number of ℓ modes to take into account.
- $\text{N_HD}, \text{N_OD}, \text{N_ID} = 100, 250, 100$. Number of grid points for the horizon, orbital and infinite domains.
- $\text{N_time}, \text{N_Fourier} = 1\,000, 40$. Number of points in time (points in orbit), and number of Fourier modes.
- $\text{field_spin}, \text{mass_ratio}, \text{particle_charge} = 0, 0.01, 1$. Spin, mass ratio, and particle charge.
- $\text{e_orbit}, \text{p_orbit} = 0.3, 7.0$. Eccentricity and semilatus rectum for the orbit (see Appendix B).
- $\text{rho_H}, \text{rho_HC}, \text{rho_HS}, \text{rho_IS}, \text{rho_IC}, \text{rho_I} = -20, -10, 0, 150, 200, 250$. Values of the compactified coordinate ρ at the nodes in Fig. (3).
- $\text{q_transition}, \text{s_transition} = 1.3, 1.5$. q and s parameters for transition function in Eq. (52).
- $\text{Mode_accuracy} = 1 \times 10^{-12}$. Desired numerical accuracy for each m -mode.

5.2 Python

We use the following Python libraries:

- `numpy`: mathematical functions and arrays.
- `scipy`: spherical harmonics and hypergeometric functions.
- `pandas`: read input parameters from CSV file.
- `argparse`: provide optional arguments.
- `logging`: event logger.
- `pickle`: store arguments into file.

5.3 Julia

In order to solve the ODEs we decide to use the Julia programming language [44]. Julia is a flexible dynamic language, with just-in-time (JIT) compilation, providing good performance, approaching that of statically compiled languages. We choose it for its `DifferentialEquations.jl` package [45], which has many robust solvers for stiff ODEs. Furthermore, it doesn't need a specific grid to ensure a given precision if no intermediate points are wanted. This is precisely the case for the compactified and transition domains, as we are only interested in the modes to compute the self-force on the particle trajectory.

We use the `py-julia` and `PyCall` packages to call Julia from Python, and Python from Julia respectively. This way, we can have the main program and modules written in Python, with only the module needed to solve the ODEs written in Julia.

With the objective of improving performance, we make use of Julia's `StaticArrays.jl` package. From the Julia documentation: "This package allows you to represent arrays in a way that avoids unnecessary heap allocations and allows the compiler to specialize code for the size of the array, e.g. by completely unrolling vector operations (eliminating the loops) and storing elements in CPU registers." Furthermore, we generate a custom system image, by building a precompiled shared library with the used packages. Thereby creating a system image that has packages embedded into the startup environment and improves startup times.

5.4 ODE example

Below, we show an example of the Julia code used to solve the ODEs in Eqs. (76) and (77):

```
w_mn = nf * PP.omega_r + mm * PP.omega_phi
# Constants needed
p = @SVector [ll, w_mn]
u0 = @SVector [1, 0, 0, -w_mn]
rspan = (PP.rho_H_plus, PP.rho_peri)
prob = ODEProblem(RHS_HD, u0, rspan, p)
sol = solve(prob, method=TRBDF2(), abstol=1e-14,
            rtol=1e-12, saveat=PP.rho_peri)
u_matrix = hcat(sol2.u...)'
R_lmn = u_matrix[:,1] + 1im * u_matrix[:,2]
Q_lmn = u_matrix[:,3] + 1im * u_matrix[:,4]
```

Where $w_{mn} = \omega_{mn}$, $ll = \ell$, and similarly for all other variables. PP is a class instance (from `class_SF_Physics.py`) with all the necessary constants and arrays needed, u0 are the boundary conditions and rspan is the range of integration. @SVector is a macro to produce a static array of type Svector. RHS_HD is a function defining the ODE for the given region. Below we show the one used for the orbital region between the pericenter and apocenter as an example:

```
function RHS_HOD(u, p, rho)
    ll, w_mn = p
    re_R, im_R, re_Q, im_Q = u
    R = re_R + 1im * im_R
    Q = re_Q + 1im * im_Q
    Vl = regge_wheeler_potential(rho, ll)
    dR = Q
    dQ = (Vl - w_mn^2) * R
    @SVector [real(dR), imag(dR), real(dQ), imag(dQ)]
end
```

Note that we use complex numbers inside the function, but transform them to two different variables for the solver to work properly.

The method used is KenCarp5, an A-L stable stiffly-accurate 5th order ESDIRK method with splitting. It includes stiffness-robust error estimates for accurate adaptive time stepping, and smoothed derivatives for highly stiff and oscillatory problems. saveat specifies the points where the solution must be stored, in this case just the endpoint, given that it will be the initial condition for the next region.

6 Results

Below we show some of the modes obtained numerically. First, in Fig. 6, we show the resulting homogeneous modes, before scaling. We can see that we obtain smooth solutions and the oscillatory behaviour is as expected for the different n and m numbers. Notice though, that the modes with $m = n = 0$ are troublesome, as they grow exponentially from infinity, as expected from Eq. (82).

These non-oscillatory modes turn out to induce instabilities in our code, making the computation of the self-force erroneous. We know this since the self-force at the particle location should be the same computed from either side, but in our code they turn out to be different. Fortunately, these modes turn out to be analytically solvable, so they can be treated separately, although we did not implement them in this present work. They can also be computed with a different method, with 2 boundary conditions, consisting on the inversion of a matricial operator (see [24]), although this method is much slower.

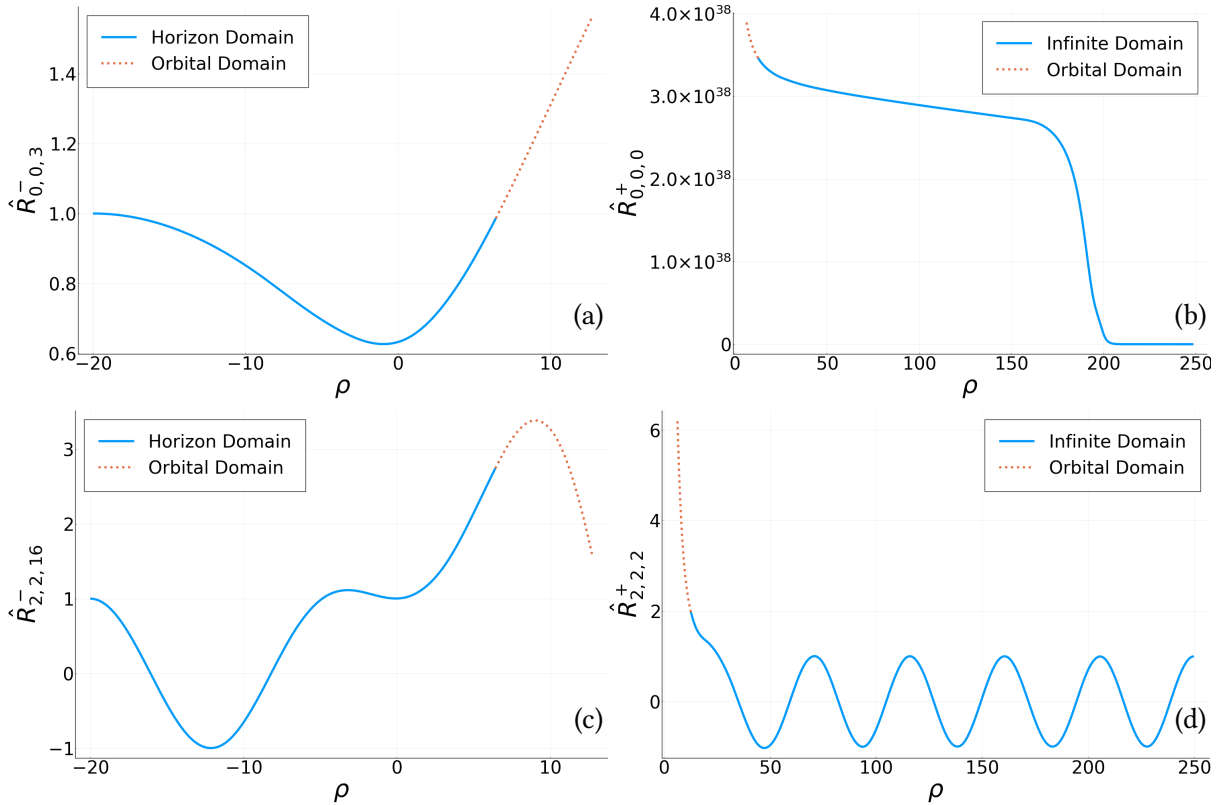


Fig. 6: Homogeneous solution $\hat{R}_{\ell m n}^{\pm}$ (real part) examples, with $\ell, m, n =$ (a) 0,0,3 at the HD, (b) 0,0,0 at the ID, note the exponential growth; (c) 2,2,16 at the HD, (d) 2,2,2 at the ID.

Next, in Fig. 7, we show the convergence of some resulting ℓm -modes after taking the sum of the Fourier series, which is approximately exponential.

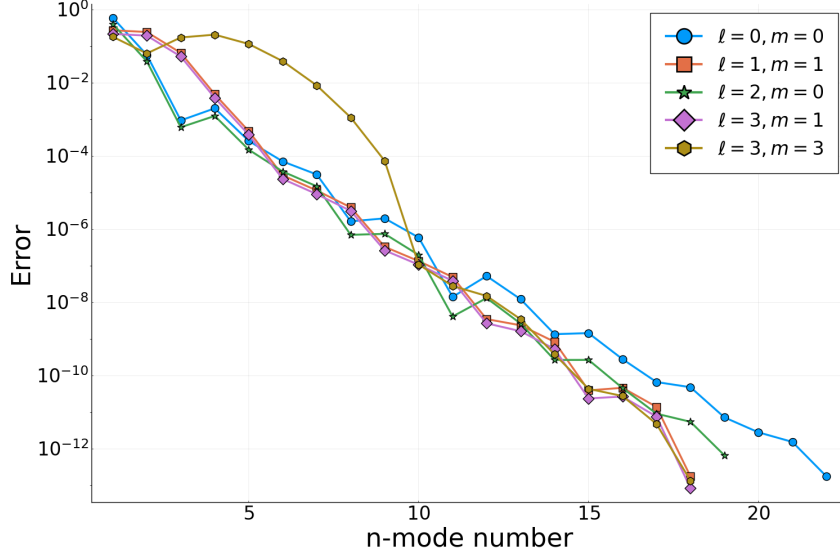


Fig. 7: Convergence of the first ℓm -modes.

7 Conclusions

The main goal of this project has been the creation of a new method for the computation of the self-force in situations of physical interest. In particular, we want to obtain the self-force for Extreme Mass Ratio Inspirals that will be observed by the future LISA observatory, in a faster manner than the state of the art. Our method is based on the PwP formulation in the frequency domain, using the case of a scalar field as a testbed for the approach, nevertheless, it is easily applicable to the gravitational case.

There are three key ingredients in our formulation. The first one is to consider a multi-domain framework in which the SCO, treated as a point particle is always located at the interface of two subdomains. Then, the equations at each subdomain become homogeneous wave equations, without distributional sources. The second is the spacetime compactification near the MBH horizon and spatial infinity, in a way that both are a finite distance away, and boundary conditions can be imposed at the two ends. Then, we get the solution for the whole spacetime region at once, instead of one point at a time. Finally, we expand the solution in both spherical harmonics and Fourier modes, so that each individual mode is smooth and

leads to fast convergence.

Once the homogeneous solution for each region $(\hat{R}_{\ell mn}^\pm, \hat{Q}_{\ell mn}^\pm)$ is obtained with arbitrary boundary conditions, we can then obtain the *real* solution $(R_{\ell mn}^\pm, Q_{\ell mn}^\pm)$ imposing the jump conditions [Eqs. (68) and (69)]. And so, adding up the modes according to Eqs. (88)-(90), we obtain the self-force at the SCO location, throughout the whole trajectory around the MBH.

We have implemented the code necessary to perform the numerical method in a combination of Python and Julia codes. The ODE solver used is based on Julia, while the main structure of the program and manipulation of the modes to obtain the self-force is done in Python. We obtain correct and smooth solutions for most of the modes. Wistfully, as we noted in the previous section, said codes do not seem to produce the right result for some modes, namely the $\ell, 0, 0$ ones, therefore a different method, either analytical or numerical should be used for those in future works.

A Spherical Harmonics

In this paper, we have followed the conventions of [46, 47]. Then, the scalar spherical harmonics are defined as

$$Y^{\ell m}(\theta, \varphi) = d_{\ell m} e^{im\varphi} = \sqrt{\frac{2\ell+1}{4\pi} \frac{(\ell-m)!}{(\ell+m)!}} P_{\ell}^m(\cos \theta) e^{im\varphi}, \quad (91)$$

where P_{ℓ}^m are the associated Legendre polynomials, defined as follows

$$P_{\ell}^m(x) = \frac{(-1)^m}{2^{\ell} \ell!} (1-x^2)^{m/2} \frac{d^{\ell+m}}{dx^{\ell+m}} (x^2-1)^{\ell}. \quad (92)$$

Three important properties of the scalar spherical harmonics are

$$\bar{Y}^{\ell m} = (-1)^m Y^{\ell -m} \quad (93)$$

$$\partial_{\varphi} Y^{\ell m} = im Y^{\ell m} \quad (94)$$

and

$$A^{\ell} \equiv \sum_{m=-\ell}^{m=\ell} A^{\ell m} Y^{\ell m} = A^{\ell 0} Y^{\ell 0} + 2 \Re \left(\sum_{m=1}^{m=\ell} A^{\ell m} Y^{\ell m} \right), \quad (95)$$

where we have assumed that the quantity A is real and hence $\bar{A}^{\ell m} = (-1)^m A^{\ell -m}$.

B Geodesic Particle motion

In this section we summarize the form of the geodesic equations for orbits around a Schwarzschild MBH that we use in this work. The four-velocity of the particle satisfies:

$$u^{\mu} = \frac{dz^{\mu}(\tau)}{d\tau}, \quad u^{\mu} \nabla_{\mu} u^{\beta} = 0. \quad (96)$$

The static and spherically symmetric character of the background imply the existence of first integrals of the motion (energy, $E_p = -u_t$, and angular momentum, $L_p = u_{\phi}$), and as it happens in the Newtonian case, the motion takes place on a plane that, without loss of generality, we can take it to be the plane $\theta = \pi/2$ ($u^{\theta} = 0$). Using the constants of motion and the normalization condition of the particle's velocity $u^{\mu}, g_{\mu\nu} u^{\mu} u^{\nu} = -1$, we can reduce the geodesic equations to first-order ODEs for (t_p, r_p, φ_p) :

$$u^t = \frac{E_p}{f}, \quad u^{\varphi} = \frac{L_p}{r^2}, \quad (u^r)^2 = E_p^2 - f \left(1 + \frac{L_p^2}{r^2} \right). \quad (97)$$

To avoid the turning points in the integration of the resulting equation for the radial coordinate, we use an angle variable that is related to the radial coordinate via

$$r_p = \frac{pM}{1 + e \cos \chi_p}, \quad (98)$$

where p is the dimensionless semilatus rectum and e is the eccentricity. From this expression, the minimum (pericenter, r_{peri}) and maximum (apocenter, r_{apo}) values of the radial coordinate, the turning points, are

$$r_{\text{peri}} = \frac{pM}{1 + e}, \quad r_{\text{apo}} = \frac{pM}{1 - e}, \quad (99)$$

and the converse:

$$pM = \frac{2 r_{\text{peri}} r_{\text{apo}}}{r_{\text{peri}} + r_{\text{apo}}}, \quad e = \frac{r_{\text{apo}} - r_{\text{peri}}}{r_{\text{peri}} + r_{\text{apo}}}. \quad (100)$$

The energy and angular momentum can be written in terms of the orbital parameters (p, e) as

$$E_p^2 = \frac{(p - 2 - 2e)(p - 2 + 2e)}{p(p - 3 - e^2)}, \quad (101)$$

$$L_p^2 = \frac{p^2 M^2}{p - 3 - e^2}. \quad (102)$$

The equations for $(\chi_p(t), \varphi_p(t))$ are

$$\frac{d\chi_p}{dt} = \frac{(p - 2 - 2e \cos \chi_p) \sqrt{p - 6 - 2e \cos \chi_p} (1 + e \cos \chi_p)^2}{Mp^2 \sqrt{(p - 2)^2 - 4e^2}}, \quad (103)$$

$$\frac{d\varphi_p}{dt} = \frac{(p - 2 - 2e \cos \chi_p) (1 + e \cos \chi_p)^2}{Mp^{3/2} \sqrt{(p - 2)^2 - 4e^2}}. \quad (104)$$

The radial period of motion and angular frequency can be obtained by using Eq. (104):

$$T_r = 2 \int_0^\pi \frac{d\chi_p}{d\chi_p/dt}, \quad \omega_r = \frac{2\pi}{T_r}. \quad (105)$$

An analysis of the geodesic motion reveals that in $\varphi_p(t)$ we can distinguish two evolution modes. One of the of secular character, increasing with time, and a second mode that is periodic in time, with period T_r . That is,

$$\varphi_p(t) = \omega_\varphi t + \Delta\varphi_p(t), \quad (106)$$

where

$$\omega_\varphi = \frac{1}{T_r} \int_0^{T_r} dt \frac{d\varphi_p(t)}{dt} = \frac{2}{T_r} \int_0^\pi d\chi_p \frac{d\varphi_p}{dt} \frac{dt}{d\chi_p} = \frac{2\sqrt{p}}{T_r} \int_0^\pi \frac{d\chi}{\sqrt{p - 6 - 2e \cos \chi}}. \quad (107)$$

An additional expression of interest is the first time derivative of the coordinate of the timelike geodesic: \dot{r}_p^* . From Eq. (97) we have

$$\dot{r}_p^* = \sqrt{1 - \frac{f_p}{E_p^2} \left(1 + \frac{L_p^2}{r_p^2}\right)}. \quad (108)$$

C Hyperboloidal Compactification Expressions

The derivatives of the compactification function $\Omega(\rho)$ are:

$$\frac{d\Omega}{d\rho} = - \left(F_T + \rho \frac{dF_T}{d\rho} \right) \frac{1}{S}, \quad (109)$$

$$\frac{d^2\Omega}{d\rho^2} = - \left(2 \frac{dF_T}{d\rho} + \rho \frac{d^2F_T}{d\rho^2} \right) \frac{1}{S}. \quad (110)$$

Where we do not specify the \pm sign that identifies the side of the compactification, since the formulas are valid for both sides. This can be used to compute the derivative of the function H :

$$\frac{dH}{d\rho} = - \frac{\Omega}{L} \left(2 \frac{d\Omega}{d\rho} + \rho \frac{\Omega}{L} \frac{d^2\Omega}{d\rho^2} \right), \quad (111)$$

where L is given in Eq. (56).

In the regions where $F_T = 1$ (near the Horizon and Spatial Infinity) we have

$$\Omega = 1 - \frac{\rho}{S}, \quad \frac{d\Omega}{d\rho} = -\frac{1}{S}, \quad \frac{d^2\Omega}{d\rho^2} = 0, \quad (112)$$

and this implies

$$L = 1. \quad (113)$$

Moreover, the function H satisfies:

$$H = 1 - \Omega^2 = \frac{\rho}{S} \left(2 - \frac{\rho}{S} \right), \quad \frac{dH}{d\rho} = \frac{2}{S} \left(1 - \frac{\rho}{S} \right). \quad (114)$$

Another expression of interest is:

$$\frac{1}{1-H} \frac{dH}{d\rho} = \frac{2}{S\Omega}. \quad (115)$$

References

- [1] B.P. Abbott et al. “Observation of Gravitational Waves from a Binary Black Hole Merger”. In: *Physical Review Letters* 116.6 (2016). issn: 1079-7114. doi: 10.1103/physrevlett.116.061102. url: <http://dx.doi.org/10.1103/PhysRevLett.116.061102> (page 4).
- [2] B.P. Abbott et al. “GWTC-1: A Gravitational-Wave Transient Catalog of Compact Binary Mergers Observed by LIGO and Virgo during the First and Second Observing Runs”. In: *Physical Review X* 9.3 (2019). issn: 2160-3308. doi: 10.1103/physrevx.9.031040. url: <http://dx.doi.org/10.1103/PhysRevX.9.031040> (page 4).
- [3] Scott A Hughes and Kip S Thorne. “Seismic gravity-gradient noise in interferometric gravitational-wave detectors”. In: *Physical Review D* 58.12 (1998), p. 122002 (page 4).
- [4] Kip S Thorne and Carolee J Winstein. “Human gravity-gradient noise in interferometric gravitational-wave detectors”. In: *Physical Review D* 60.8 (1999), p. 082001 (page 4).
- [5] KAGRA Collaboration and T. Akutsu. *Overview of KAGRA : KAGRA science*. 2020. arXiv: 2008.02921 [gr-qc] (page 4).
- [6] M Punturo, M Abernathy, F Acernese, B Allen, Nils Andersson, K Arun, F Barone, B Barr, M Barsuglia, M Beker, et al. “The Einstein Telescope: a third-generation gravitational wave observatory”. In: *Classical and Quantum Gravity* 27.19 (2010), p. 194002 (page 4).
- [7] Pau Amaro-Seoane et al. “Laser Interferometer Space Antenna”. In: (2017). arXiv: 1702.00786 [astro-ph.IM] (pages 4, 5).
- [8] Pau Amaro-Seoane, Jonathan R. Gair, Adam Pound, Scott A. Hughes, and Carlos F. Sopuerta. “Research Update on Extreme-Mass-Ratio Inspirals”. In: (2014). arXiv: 1410.0958 [astro-ph.CO] (pages 4, 5).
- [9] Stanislav Babak, Jonathan Gair, Alberto Sesana, Enrico Barausse, Carlos F. Sopuerta, Christopher P. L. Berry, Emanuele Berti, Pau Amaro-Seoane, Antoine Petiteau, and Antoine Klein. “Science with the space-based interferometer LISA. V: Extreme mass-ratio inspirals”. In: *Phys. Rev. D* 95.10 (2017), p. 103012. doi: 10.1103/PhysRevD.95.103012. arXiv: 1703.09722 [gr-qc] (pages 4, 5).
- [10] Christopher P. L. Berry, Scott A. Hughes, Carlos F. Sopuerta, Alvin J. K. Chua, Anna Hefernan, Kelly Holley-Bockelmann, Deyan P. Mihaylov, M. Coleman Miller, and Alberto Sesana. “The unique potential of extreme mass-ratio inspirals for gravitational-wave astronomy”. In: (2019). arXiv: 1903.03686 [astro-ph.HE] (pages 4, 5).
- [11] Leor Barack et al. “Black holes, gravitational waves and fundamental physics: a roadmap”. In: *Class. Quant. Grav.* 36.14 (2019), p. 143001. doi: 10.1088/1361-6382/ab0587. arXiv: 1806.05195 [gr-qc] (page 5).
- [12] Enrico Barausse et al. “Prospects for Fundamental Physics with LISA”. In: (2020). arXiv: 2001.09793 [gr-qc] (page 5).
- [13] Carlos F. Sopuerta. “A Roadmap to Fundamental Physics from LISA EMRI Observations”. In: *GW Notes* 4 (4 2010), pp. 3–47. arXiv: 1009.1402 [astro-ph.CO] (page 5).
- [14] Eric Poisson. “The motion of point particles in curved spacetime”. In: *Living Rev. Relativity* 7 (2004), p. 6. eprint: gr-qc/0306052. url: <http://www.livingreviews.org/lrr-2004-6> (pages 5, 7).
- [15] Yasushi Mino, Misao Sasaki, and Takahiro Tanaka. “Gravitational radiation reaction to a particle motion”. In: *Phys.Rev. D* 55 (1997), pp. 3457–3476. arXiv: gr-qc/9606018 (page 5).
- [16] Theodore C. Quinn and Robert M. Wald. “An axiomatic approach to electromagnetic and gravitational radiation reaction of particles in curved spacetime”. In: *Phys.Rev. D* 56 (1997), pp. 3381–3394. arXiv: gr-qc/9610053 (page 5).

- [17] Leor Barack and Amos Ori. “Mode sum regularization approach for the self force in black hole spacetime”. In: *Phys.Rev. D* 61 (2000), p. 061502. eprint: gr-qc/9912010 (pages 5, 9).
- [18] Leor Barack. “Self-force on a scalar particle in spherically-symmetric spacetime via mode-sum regularization: Radial trajectories”. In: *Phys.Rev. D* 62 (2000), p. 084027. arXiv: gr-qc/0005042 (page 5).
- [19] Leor Barack. “Gravitational self-force by mode sum regularization”. In: *Phys.Rev. D* 64 (2001), p. 084021. arXiv: gr-qc/0105040 (page 5).
- [20] Leor Barack, Yasushi Mino, Hiroyuki Nakano, Amos Ori, and Misao Sasaki. “Calculating the gravitational self force in Schwarzschild spacetime”. In: *Phys.Rev.Lett.* 88 (2002), p. 091101. arXiv: gr-qc/0111001 (pages 5, 9).
- [21] Luis Lehner. “Numerical relativity: a review”. In: *Classical and Quantum Gravity* 18.17 (2001), R25 (page 6).
- [22] C. V. Vishveshwara. “Stability of the Schwarzschild metric”. In: *Phys. Rev. D* 1 (1970), pp. 2870–2879 (page 6).
- [23] S. Chandrasekhar and Steven L. Detweiler. “The quasi-normal modes of the Schwarzschild black hole”. In: *Proc. Roy. Soc. Lond. A* 344 (1975), pp. 441–452. doi: 10.1098/rspa.1975.0112 (page 6).
- [24] Priscilla Canizares and Carlos F. Sopuerta. “An Efficient Pseudospectral Method for the Computation of the Self-force on a Charged Particle: Circular Geodesics around a Schwarzschild Black Hole”. In: *Phys.Rev. D* 79 (2009), p. 084020. doi: 10.1103/PhysRevD.79.084020. arXiv: 0903.0505 [gr-qc] (pages 6, 10, 29).
- [25] Priscilla Canizares, Carlos F. Sopuerta, and Jose Luis Jaramillo. “Pseudospectral Collocation Methods for the Computation of the Self-Force on a Charged Particle: Generic Orbits around a Schwarzschild Black Hole”. In: *Phys.Rev. D* 82 (2010), p. 044023. doi: 10.1103/PhysRevD.82.044023. arXiv: 1006.3201 [gr-qc] (pages 6, 9, 10).
- [26] Priscilla Canizares and Carlos F. Sopuerta. “Tuning Time-Domain Pseudospectral Computations of the Self-Force on a Charged Scalar Particle”. In: *Class.Quant.Grav.* 28 (2011), p. 134011. doi: 10.1088/0264-9381/28/13/134011. arXiv: 1101.2526 [gr-qc] (pages 6, 10).
- [27] Jose Luis Jaramillo, Carlos F. Sopuerta, and Priscilla Canizares. “Are Time-Domain Self-Force Calculations Contaminated by Jost Solutions?” In: *Phys.Rev. D* 83 (2011), p. 061503. doi: 10.1103/PhysRevD.83.061503. arXiv: 1101.2324 [gr-qc] (page 6).
- [28] Priscilla Canizares and Carlos F. Sopuerta. “Overcoming the Gauge Problem for the Gravitational Self-Force”. In: (2014). arXiv: 1406.7154 [gr-qc] (page 6).
- [29] Marius Oltean, Carlos F. Sopuerta, and Alessandro D.A.M. Spallicci. “Particle-without-Particle: a practical pseudospectral collocation method for linear partial differential equations with distributional sources”. In: *J. Sci. Comput.* 79 (2019), p. 827. doi: 10.1007/s10915-018-0873-9. arXiv: 1802.03405 [physics.comp-ph] (pages 6, 10).
- [30] Carlos F. Sopuerta, Pengtao Sun, Pablo Laguna, and Jinchao Xu. “A Toy model for testing finite element methods to simulate extreme-mass-ratio binary systems”. In: *Class.Quant.Grav.* 23 (2006), pp. 251–286. doi: 10.1088/0264-9381/23/1/013. arXiv: gr-qc/0507112 (page 6).
- [31] Carlos F. Sopuerta and Pablo Laguna. “Finite element computation of the gravitational radiation emitted by a point-like object orbiting a non-rotating black hole”. In: *Phys. Rev. D* 73 (2006), p. 044028. eprint: gr-qc/0512028 (page 6).
- [32] Steven Detweiler and Bernard F. Whiting. “Self-force via a Green’s function decomposition”. In: *Phys.Rev. D* 67 (2003), p. 024025. arXiv: gr-qc/0202086 (page 8).

- [33] T. Regge and J. A. Wheeler. “Stability of a Schwarzschild Singularity”. In: *Phys. Rev.* 108 (Nov. 1957), pp. 1063–1069. doi: 10.1103/PhysRev.108.1063 (page 8).
- [34] Leor Barack and Amos Ori. “Regularization parameters for the self force in Schwarzschild spacetime. I: Scalar case”. In: *Phys.Rev. D* 66 (2002), p. 084022. doi: 10.1103/PhysRevD.66.084022. arXiv: gr-qc/0204093 (page 9).
- [35] Dong-Hoon Kim. “Regularization parameters for the self-force of a scalar particle in a general orbit about a Schwarzschild black hole”. In: (2004). arXiv: gr-qc/0402014 (page 9).
- [36] Dong-Hoon Kim. “Radiation Reaction in Curved Spacetime”. PhD thesis. University of Florida, 2005 (page 9).
- [37] Roland Haas and Eric Poisson. “Mode-sum regularization of the scalar self-force: Formulation in terms of a tetrad decomposition of the singular field”. In: *Phys.Rev. D* 74 (2006), p. 044009. doi: 10.1103/PhysRevD.74.044009. arXiv: gr-qc/0605077 (page 9).
- [38] Leor Barack, Amos Ori, and Norichika Sago. “Frequency-domain calculation of the self force: The High-frequency problem and its resolution”. In: *Phys.Rev. D* 78 (2008), p. 084021. doi: 10.1103/PhysRevD.78.084021. arXiv: 0808.2315 [gr-qc] (pages 15, 19, 20).
- [39] Anil Zenginoglu. “Hyperboloidal layers for hyperbolic equations on unbounded domains”. In: *J.Comput.Phys.* 230 (2011), pp. 2286–2302. doi: 10.1016/j.jcp.2010.12.016. arXiv: 1008.3809 [math.NA] (pages 15, 16).
- [40] C. E. Grosch and S. A. Orszag. “Numerical solution of Problems in Unbounded Regions: Coordinate Transforms”. In: *J.Comput.Phys.* 25 (1977), pp. 273–296 (page 16).
- [41] Frans Pretorius. “Numerical relativity using a generalized harmonic decomposition”. In: *Class.Quant.Grav.* 22 (2005), pp. 425–452. doi: 10.1088/0264-9381/22/2/014. arXiv: gr-qc/0407110 (page 16).
- [42] Sebastiano Bernuzzi, Alessandro Nagar, and Anil Zenginoglu. “Horizon-absorption effects in coalescing black-hole binaries: An effective-one-body study of the non-spinning case”. In: *Phys.Rev. D* 86 (2012), p. 104038. doi: 10.1103/PhysRevD.86.104038. arXiv: 1207.0769 [gr-qc] (page 18).
- [43] Nicolas Yunes, Wolfgang Tichy, Benjamin J. Owen, and Bernd Bruegmann. “Binary black hole initial data from matched asymptotic expansions”. In: *Phys.Rev. D* 74 (2006), p. 104011. doi: 10.1103/PhysRevD.74.104011. arXiv: gr-qc/0503011 (page 18).
- [44] Jeff Bezanson, Alan Edelman, Stefan Karpinski, and Viral B Shah. “Julia: A fresh approach to numerical computing”. In: *SIAM Review* 59.1 (2017), pp. 65–98. doi: 10.1137/141000671 (page 27).
- [45] Christopher Rackauckas and Qing Nie. “DifferentialEquations.jl—a performant and feature-rich ecosystem for solving differential equations in julia”. In: *Journal of Open Research Software* 5.1 (2017) (page 27).
- [46] M. Abramowitz and I. A. Stegun. *Handbook of Mathematical Functions with Formulas, Graphs, and Mathematical Tables*. New York: Dover, 1972 (page 32).
- [47] William H. Press, Brian P. Flannery, Saul A. Teukolsky, and William T. Vetterling. *Numerical Recipes: The Art of Scientific Computing*. Cambridge (UK) and New York: Cambridge University Press, 1992 (page 32).